










Eccentric Dust Ring in the IRS 48 Transition Disk

Haifeng Yang (杨海峰)^{1,6} , Manuel Fernández-López² , Zhi-Yun Li³ , Ian W. Stephens⁴ , Leslie W. Looney⁵ ,
Zhe-Yu Daniel Lin³ , and Rachel Harrison⁵ 

¹ Kavli Institute for Astronomy and Astrophysics, Peking University, Yi He Yuan Lu 5, Haidian Qu, Beijing 100871, People's Republic of China
hfyang@pku.edu.cn

² Instituto Argentino de Radioastronomía (CCT-La Plata, CONICET; CICPBA), C.C. No. 5, 1894, Villa Elisa, Buenos Aires, Argentina

³ Department of Astronomy, University of Virginia, Charlottesville, VA 22903, USA

⁴ Department of Earth, Environment, and Physics, Worcester State University, Worcester, MA 01602, USA

⁵ Department of Astronomy, University of Illinois, 1002 West Green Street, Urbana, IL 61801, USA

Received 2022 December 5; revised 2023 March 19; accepted 2023 April 4; published 2023 April 26

Abstract

Crescent-shaped structures in transition disks hold the key to studying the putative companions to the central stars. The dust dynamics, especially that of different grain sizes, is important to understanding the role of pressure bumps in planet formation. In this work, we present deep dust continuum observation with high resolution toward the Oph IRS 48 system. For the first time, we are able to significantly trace and detect emission along 95% of the ring crossing the crescent-shaped structure. The ring is highly eccentric with an eccentricity of 0.27. The flux density contrast between the peak of the flux and its counterpart along the ring is ~ 270 . In addition, we detect a compact emission toward the central star. If the emission is an inner circumstellar disk inside the cavity, it has a radius of at most a couple of astronomical units with a dust mass of $1.5 \times 10^{-8} M_{\odot}$, or $0.005 M_{\oplus}$. We also discuss the implications of the potential eccentric orbit on the proper motion of the crescent, the putative secondary companion, and the asymmetry in velocity maps.

Unified Astronomy Thesaurus concepts: Dust continuum emission (412); Interferometry (808); Interplanetary dust (821); Protoplanetary disks (1300); Submillimeter astronomy (1647)

1. Introduction

Transition disks (TD) are protoplanetary disks with large inner cavities. These cleared inner regions hint at the existence of a companion (e.g., Marsh & Mahoney 1992) or a history of photoevaporation (e.g., Alexander et al. 2014 and references therein). The Atacama Large Millimeter/submillimeter Array (ALMA) has revealed many transition disks with diverse structures (see van der Marel et al. 2021a and reference therein). Among these structures, the crescent-shaped structures are of particular interest, because they directly link to the putative companion. Theoretically, the creation of such structures have at least three possible origins. A crescent can be a long-lived vortex caused by Rossby wave instability (RWI; Zhu et al. 2014) or a dust horseshoe from the overdensity at the cavity edge (Ragusa et al. 2017). The crescent-shaped structures from these two mechanisms are triggered by companions but of different masses (Dong et al. 2018; Ragusa et al. 2020). They move at the local Keplerian speed and both cause azimuthal dust segregation (Birnstiel et al. 2013). The third mechanism relies on the eccentric disk caused by a massive companion (Kley & Dirksen 2006; Ataiee et al. 2013). In this case, an eccentric disk induced by a companion has an overdense region near the apocenter, which manifests itself as a slowly precessing crescent-shaped structure with a negligible proper motion.

Among all transition disks, Oph IRS 48 stands out and draws interest and studies for several reasons. It has a prominent crescent-shaped structure with a density contrast of > 100 , but only at (sub)millimeter wavelengths (van der Marel et al. 2013). On the contrary, the mid-IR and ^{12}CO line emissions both show symmetric structures (van der Marel et al. 2013). In addition, the azimuthal concentration increases toward longer wavelengths (van der Marel et al. 2015), hinting at dust segregation of different grain sizes, which supports the vortex picture (Zhu et al. 2014).

In addition to the crescent-shaped structures, some transition disks may have hot dust near the central star or even resolved inner disks. They have a substantial infrared excess and are classified as pretransitional disks (PTDs), an intermediate state between full disks and transitional disks (Espaillat et al. 2010, 2014).⁷ Whether IRS 48 is a PTD or TD is uncertain due to the presence of strong polycyclic aromatic hydrocarbon emission (Geers et al. 2007), even though it has 3.8% near-infrared (NIR) excess (Francis & van der Marel 2020). Previous observations did not resolve the putative inner disk associated with the infrared excess, and gave an upper limit of the dust mass of $0.009 M_{\oplus}$ (Francis & van der Marel 2020). At the same time, IRS 48 has an appreciable mass accretion rate of $10^{-8.4} M_{\odot} \text{ yr}^{-1}$ (Salyk et al. 2013). A detection of the inner disk in the IRS 48 system will confirm its classification as a PTD, and help us understand the evolution of transition disks.

In this work, we present new deep observations toward IRS 48 with high resolution. The structure of the paper is as follows. In Section 2, we discuss the observation and data reduction. In Section 3, we discuss the main features of the

⁶ Boya Fellow.

⁷ Recently, Francis & van der Marel (2020) showed that there is no clear correlation between NIR excess and central millimeter-dust emission. The PTD/TD classification is currently under debate.

data: an eccentric ring and the detection of dust emission inside the cavity. In Section 4, we discuss the proper motion and the physics behind the eccentric ring. We present our conclusions in Section 5.

2. Observations

Observations were conducted on 2021 June 7, June 14, and July 19 using ALMA Band 7 (0.87 mm) under the project code 2019.1.01059.S (PI: H. Yang). ALMA used 42–46 antennas in six execution blocks (approximately 1.75 hr each) in two different array configurations (C43-6 and C43-7), which together provided baselines ranging from 15 to 3700 m. Weather conditions were good for 0.87 mm observations. The mean precipitable water vapor column ranged between 0.6 and 0.9 mm, and the system temperature were between 132 and 171 K. The experiment was primarily designed for studying the polarization of the dust emission toward IRS 48. Hence, we tuned four ALMA basebands dedicated for the dust continuum emission, centered at 336.5, 338.4, 348.5, and 350.5 GHz, all having a nominal 2.0 GHz bandwidth. The observations toward IRS 48 were intertwined with visits to the phase and the polarization calibrators every ~ 4 and ~ 40 minutes, respectively. The observations include also periodic visits to a check source (quasar J1647-2912) every 15 minutes. The total integrated time over IRS 48 was 3.8 hr, and there was sufficient parallactic angle coverage for polarization calibration. The phase center was located at $(\alpha, \delta)_{\text{ICRS}} = (16^{\text{h}}27^{\text{m}}37^{\text{s}}190, -24^{\circ}30'35''030)$. The calibration by the ALMA staff was produced using the Common Astronomy Software Applications (CASA) package version v6.2.1.7 (McMullin et al. 2007) in the delivered data. J1337-1257 and J1517-2422 were used as the flux and bandpass calibrators on different days; J1700-2610 and J1647-2912 were the phase calibrators (average fluxes of 0.94 and 0.097 Jy, respectively); J1733-1304 was the polarization calibrator in all execution blocks. ALMA Band 7 observations have a typical absolute flux uncertainty of 10%, and the polarization uncertainties are usually constraint by the gain leakages, which are less than 5%. The images of the continuum were also made using CASA. To construct them we combined the four continuum basebands avoiding some spectral channels with potential line emission (C^{17}O (3-2) and several CH_3OH transitions). We ran two phase-only self-calibration iterations on the continuum Stokes I data. The solution intervals used for the first and second were infinite (i.e., a solution interval over the whole data set) and 25 s, respectively. The final signal-to-noise ratio (S/N) of the Stokes I image is just above 1250. The self-calibration solutions from the continuum Stokes I were then applied to the continuum Stokes QUV. To clean the images, we use the CASA task `tclean` using the Hogbom algorithm with a Briggs weighting of 0.5. The final continuum synthesized beam is $0''.11 \times 0''.072$, with a position angle of -73° . Note that, in this case, the self-calibration did not affect the positional accuracy. The difference between the measured peak positions before and after self-calibration are well within astrometric accuracy. The rms noise level measured in the Stokes I image is $14 \mu\text{Jy}$. For the Stokes QUV images the rms noise level is $12 \mu\text{Jy}$. The Letter focuses on the features in the Stokes I data; the polarization data will be discussed elsewhere.

We use the parallax, the proper motion, and the location of the IRS 48 star from Gaia DR3 (Gaia Collaboration et al. 2022). From the parallax, we derive a distance of 136 pc, which

is slightly different from the distance, 134 pc, inferred from Gaia DR2 data (Gaia Collaboration et al. 2018; van der Marel et al. 2021b). According to the Gaia DR3, in the year 2016, the star is at $(16^{\text{h}}27^{\text{m}}37^{\text{s}}180, -24^{\circ}30'35''416)$. It has an proper motion of $-8.72 \text{ mas yr}^{-1}$ in R.A. and $-24.4 \text{ mas yr}^{-1}$ in decl. We derived the location at the time of our observation as $(16^{\text{h}}27^{\text{m}}37^{\text{s}}177, -24^{\circ}30'35''550)$, assuming a 5.5 yr time difference. This will be the center of all images in this paper.

3. Results

The primary-beam-corrected dust continuum image from our observation is shown in Figure 1. The peak of the emission has 1285 S/N or $18.00 \text{ mJy beam}^{-1}$. In addition to the well-known crescent-shaped structure, we also detect a long tail of dust emission trailing behind the crescent-shaped structure, with respect to the counterclockwise rotation of the disk (Bruderer et al. 2014), and some diffuse emission with over 3σ detection in the northwest part of the disk. These two structures form an ellipse around the central object and will be discussed in Section 3.1. We also detect some emission at the 15σ level near the central object and separate it from the outer crescent for the first time. We will discuss this emission in Section 3.2.

3.1. Eccentric Ring

Our ALMA observations are the deepest high-resolution (sub)millimeter observations toward IRS 48 to date, reaching a noise level of $14 \mu\text{Jy/beam}$ at an angular resolution of $0''.11 \times 0''.072$. For the first time we are able to significantly trace and detect emission from about 95% of the ring crossing the crescent-shaped structure. Assuming an inclination angle of 50° and a position angle of 100° (Bruderer et al. 2014), we deproject the image to the disk plane. The results are shown in the left panel of Figure 2. We can see that the north–northwest tail behind the crescent-shaped structure and the diffuse emission in the northwest part of the disk structure form an elliptical pattern rather than a circular pattern.

To fit the elliptical ring, we first parameterize the ellipse with the semimajor axis a , the eccentricity e , and the position angle of the major axis of the ellipse. We fix one of the foci on the central star. The fitting is done on the deprojected image, and the loss function is defined as $\mathcal{L} \equiv \sum I(x, y) f(dr(x, y))$, where $I(x, y)$ is the intensity and $dr(x, y)$ is the difference of the radial distance from the center between the point in the image and the target ellipse. The $f(dr)$ function is defined as

$$f(dr) = \begin{cases} (dr/\delta_p)^2 & dr \leq 0 \\ (1.5dr/\delta_p)^2 & dr > 0 \end{cases}, \quad (1)$$

where $\delta_p = 0''.02$ is about the pixel size of our image, or $1/5$ of the beam size. The choice of δ_p and the prefactor are arbitrary as we minimize the loss function to get the best-fitted model. The loss function is engineered to have our fitted ellipse crossing the central peak of the crescent-shaped structure, as the one we present in the next paragraph.

The best fit is plotted as a colored ellipse in Figure 2 with the color representing the ratio of the orbital velocity to the local Keplerian velocity⁸ v/v_K . The best fit has a semimajor axis

⁸ Given semimajor axis a and the distance to the center r , the ratio of the orbital velocity along elliptical orbit to the Keplerian velocity assuming circular orbit with a radius of r is $v/v_K = \sqrt{2 - (r/a)^2}$.

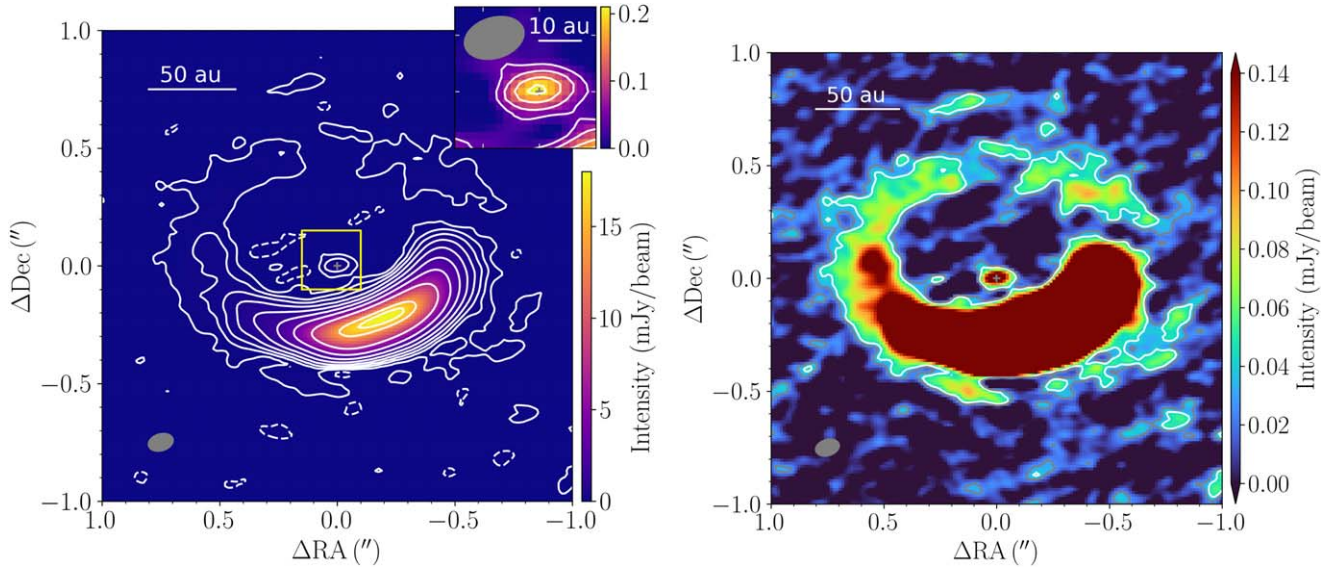


Figure 1. Left: the synthesized dust continuum image of IRS 48 at $870\ \mu\text{m}$ or $345\ \text{GHz}$. Both the color map and the contours represent the flux density in mJy beam^{-1} . The contours are plotted at the levels of $(-3, 3, 8, 16, 64, 128, 256, 512, 1024, 1200) \times \sigma$, where $\sigma = 14\ \mu\text{Jy beam}^{-1}$ is the rms noise. The synthesized beam is $0''.11 \times 0''.072$. The inset shows a $0''.15$ wide zoom, with contours representing the flux density at the levels of $(3, 6, 10, 14) \times \sigma$. The star location is labeled as a gray cross. Right: the same image but with a different color map with a maximum value $0.14\ \text{mJy beam}^{-1}$, 10σ , to saturate the crescent-shaped structure and display the dim long tail better. The white and gray contours correspond to flux densities of 3σ and 2σ , respectively.

$a = 0''.57$, or $78\ \text{au}$, and an eccentricity $e = 0.27$. At the perihelion, the velocity is about $1.13v_K$, which is slightly super Keplerian. We will discuss the implication of the elliptical dust distribution in more detail in Section 4.1.

In the bottom right panel, we plot the same deprojected image in the (r, θ) coordinates. The θ is defined such that the perihelion corresponds to $\theta = 180^\circ$. Note that a circular orbit is a horizontal straight line in these coordinates. Our fitted ellipse is very eccentric with an aphelion to perihelion distance ratio of 1.78. In the top right panel, we plot the flux density profile in logarithmic scale along the fitted ellipse. We can see that the density structure is not symmetric with respect to the peak, and it resembles a droplet or a tadpole. The head is rounder with about 90° spread in azimuthal angle whereas the tail spreads over almost 180° . The diffuse emission in the northwest part of the disk has an azimuthal extent of 40° – 50° . Since the emission along part of the ellipse is not robustly detected, the ratio of the maximum intensity is at least 400 times the minimum. As a reference for interested readers, the flux density contrast of the peak with the point along the ring with 180° position angle difference is 271.

The necessity for the ring to be eccentric is clear given that the north part is ~ 1.8 times further from the central star than the peak, and the exact value of the inclination angles does not change the eccentricity too much, as long as the position angle of the disk is fixed. From the left panel of Figure 2, we can see that the major axis of the ellipse is very close to being vertical. In this case, changing the inclination angle will change both the apocenter and pericenter distances by the same factor, leaving the ratio unchanged as ~ 1.8 . The semimajor axis will be different for the new inclination angle, but the eccentricity can be inferred directly as $e \approx (1.8-1)/(1.8+1) \approx 0.28$. So the eccentricity does not depend on the adopted inclination angle too much. The assumption of the central star as one focus has a much larger impact on the eccentricity. We will discuss these possibilities in more detail in Section 4.2.

3.2. Detection of Central Emission

Figure 1 clearly shows a central source with at least 3σ emission over more than two beams. This source has a peak flux density of $0.21\ \text{mJy beam}^{-1}$, at an S/N level 15σ . We conduct a simple 2D-Gaussian fit to this central continuum emission. The center is only 3 mas west of the central star, well within one pixel of our image (20 mas). The spatial coincidence between the star location inferred from the Gaia data and the center of the central emission adds confidence to the location determination to both of them. It also makes it unlikely for this source to be either background contamination or random calibration or cleaning artifact. The major and minor axis of the 2D-Gaussian fit is $0''.095 \times 0''.052$, which is smaller than our beam size. Even though the 3σ contour is larger than two beams, our data are still in agreement with a point source.

The simplest assumption is that this central emission comes from dust. However, before calculating a dust mass about the central source, we explore whether this emission may come from other sources. First, the central emission cannot be completely explained by emission coming from a central star. The star IRS 48 was estimated as a $2 M_\odot$ star using kinematic modeling (Brown et al. 2012). The effective temperature and the bolometric luminosity was estimated as 9520 K and $17.8 L_\odot$ (Brown et al. 2012; rescaled by Francis & van der Marel 2020 using new distance from Gaia DR2 data, Gaia Collaboration et al. 2018). The effective temperature and the bolometric luminosity combined yield a radius of $1.55 R_\odot$. We can then calculate the flux density at the wavelength of $870\ \mu\text{m}$ as $7.22 \times 10^{-6}\ \text{Jy}$. This is 21 times smaller than what we detect.

Another possibility to explain the central unresolved emission is that it comes from the free-free emission of an ionized wind. Taking the flux of the central source at 34 GHz ($36\ \mu\text{Jy}$, van der Marel et al. 2015) and the flux derived in our 2D-Gaussian fit at $343.5\ \text{GHz}$ ($221\ \mu\text{Jy}$), we obtain a spectral index of 0.78 ± 0.20 . This spectral index is consistent with the partially optically thick free-free emission of a jet/wind.

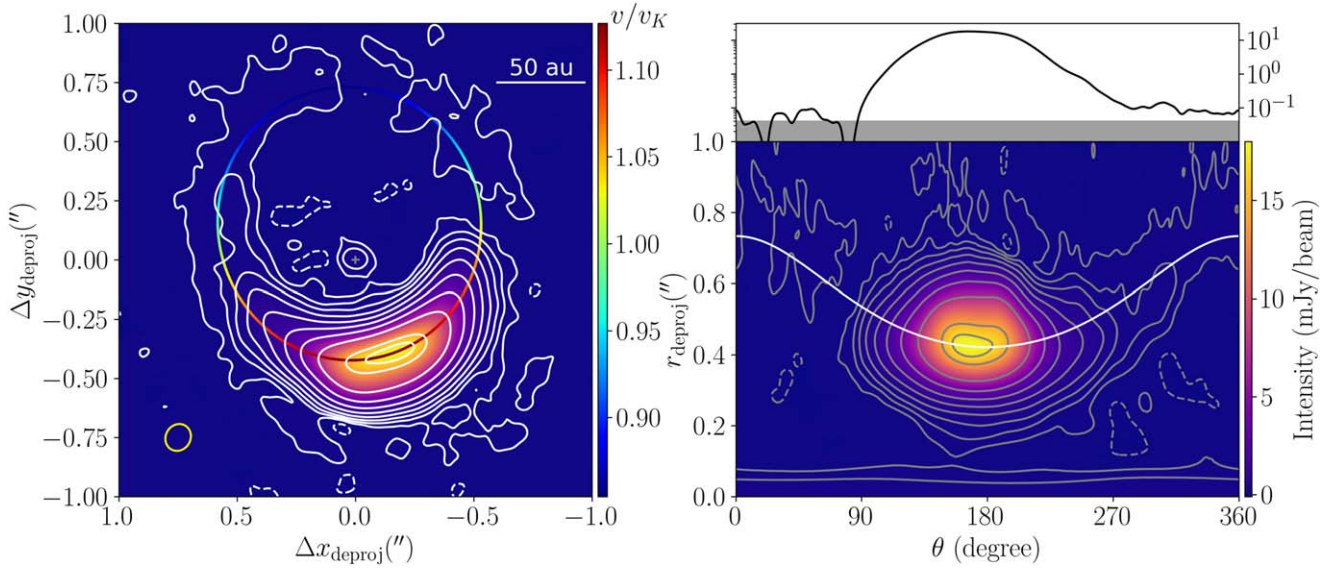


Figure 2. Left: the fitted elliptical ring in the deprojected view. The image shares the color bar with the bottom right panel. The central star (gray cross; derived from Gaia DR3) is assumed to be one of the foci. The contours are plotted at the same levels as in Figure 1. The colored ellipse shows the best-fitted ring, with colors representing the ratio of the orbital velocity to the local Keplerian velocity, v/v_K on the color bar. The yellow ellipse at the lower left corner shows the synthetic beam deprojected to the disk plane. Bottom right: the deprojected image in (r, θ) coordinates, where $\theta = 0$ corresponds to the aphelion of the best-fitted elliptical ring. Note that a circular orbit is a straight horizontal line in this view. Top right: the flux density along the best-fitted elliptical ring in logarithmic scale. It shares the x -axis with the panel below. The gray contours are plotted at the same levels as in Figure 1.

Although ionized jets are common among young stars the turnover frequency from the partially optically thick to the optically thin regimes depends upon the ionized gas density at the jet base and it is usually located at the centimeter part of the continuum spectrum (e.g., Reynolds 1986; Mohan et al. 2022). Therefore, if the emission of the central source at 343.5 GHz has a contribution from a thermal ionized jet, it would most probably be in the optically thin regime, with a spectral index of -0.1 . Assuming that the emission of a thermal jet is optically thin from 34 to 343.5 GHz, the free-free contribution would be $29 \mu\text{Jy}$ at 343.5 GHz, roughly 10 times smaller than the measured flux.

Neither the emission from the protostellar photosphere, nor the emission from an ionized wind could alone (or added) explain the measured flux from the central source in the ALMA image. Still other possible contributions can be due to the nonthermal synchrotron emission from the protostellar magnetosphere (Andre & Yau 1997), the ionized emission from the dust sublimation wall (e.g., Añez-López et al. 2020), or the collisions from pebbles and planetesimals that heat the dust of a disk (such as proposed in Vega, Matrà et al. 2020). The former two hypotheses are expected to be more prominent in the centimeter wavelength range, while the third hypothesis is somehow a more exotic solution that may need more theoretical work to be supported. In this work we will assume a more simple hypothesis, in which most of the submillimeter emission comes from the thermal dust emission of an inner disk. Following this idea, we can put a constraint on the dust mass of the central object. The mean flux density within the 3σ contour is about $8.65 \times 10^{-5} \text{ Jy beam}^{-1}$, corresponding to a brightness temperature of 0.164 K. This is extremely optically thin for any reasonable dust temperature. The area of this region is measured as 291 au^2 . Given the small size of the central source (maximum distance from the central star is $\sim 10 \text{ au}$), we assume a dust temperature of 100 K. We also assume a dust opacity of $3.5 \text{ cm}^2 \text{ g}^{-1}$, which is the fiducial dust

model from Birnstiel et al. (2018) with 1 mm maximum grain size at $870 \mu\text{m}$ wavelength. Under these assumptions, the dust mass is estimated to be about $1.5 \times 10^{-8} M_{\odot}$, or $0.005 M_{\oplus}$.

4. Discussion

4.1. Proper Motion

In Section 3.1, we fit the ring crossing the crescent-shaped structure with an elliptical orbit having an eccentricity of 0.27, and the current peak of the crescent-shaped structure is near the perihelion of the orbit. Such an eccentric orbit would have a local velocity near the perihelion of about $1.13v_K$. The crescent-shaped structure following this orbit should also move at a super Keplerian speed.

Since van der Marel et al. (2013), the IRS 48 has been observed with ALMA at high resolution multiple times (van der Marel et al. 2015; Francis & van der Marel 2020; van der Marel et al. 2021b; 2021 observations in this study). The 9 yr separation in observing time allows us to constrain the proper motion of the crescent-shaped structure. We obtained the archival ALMA data and use CASA `imfit` to conduct 2D-Gaussian fit to the crescent. The observation time, adopted epoch, observing band, beam size, astrometric error δ_{astro} , `imfit` results, and references are presented in Table 1. When estimating the astrometric error, we followed the ALMA Technical Handbook,⁹ which is the beam size divided by the S/N (saturates in 20) divided by 0.9. For observations with resolution finer than $0''.15$, the positional error can be up to a factor of 2 higher. Only our observations are this high resolution, so we doubled the aforementioned astrometric error to be conservative. For the `imfit` results, we present the fitted peak location translated to the International Celestial Reference System (ICRS) frame, the error in R.A. and the error in decl. The locations of the peaks are plotted in panels (a) and (c) in

⁹ Section 10.5.2 of ALMA Technical Handbook (Cycle 9). <https://almascience.nrao.edu/proposing/technical-handbook>.

Table 1
The Proper Motion of the Peak of the Crescent-shaped Structure

Observation Time	Epoch	Band	Beam Size	$\delta_{\text{astro}}(^{\prime\prime})$	Peak Location (ICRS)	$\delta_{\text{R.A.}}(^{\prime\prime})$	$\delta_{\text{decl.}}(^{\prime\prime})$	References
06/2012; 07/2012	2012.50	9	$0^{\prime\prime}.32 \times 0^{\prime\prime}.21$	0.018	$16^{\text{h}}27^{\text{m}}37^{\text{s}} 172, -24^{\circ}30^{\prime}35^{\prime\prime} 593$	0.0075	0.0024	1
06/2014	2014.45	9	$0^{\prime\prime}.19 \times 0^{\prime\prime}.14$	0.011	$16^{\text{h}}27^{\text{m}}37^{\text{s}} 169, -24^{\circ}30^{\prime}35^{\prime\prime} 628$	0.0139	0.0049	2
07/2015; 08/2015	2015.58	7	$0^{\prime\prime}.18 \times 0^{\prime\prime}.12$	0.010	$16^{\text{h}}27^{\text{m}}37^{\text{s}} 167, -24^{\circ}30^{\prime}35^{\prime\prime} 684$	0.0070	0.0026	3
08/2018	2018.63	7	$0^{\prime\prime}.49 \times 0^{\prime\prime}.39$	0.027	$16^{\text{h}}27^{\text{m}}37^{\text{s}} 166, -24^{\circ}30^{\prime}35^{\prime\prime} 745$	0.0031	0.0015	4
06/2021; 07/2021	2021.50	7	$0^{\prime\prime}.11 \times 0^{\prime\prime}.072$	0.012	$16^{\text{h}}27^{\text{m}}37^{\text{s}} 163, -24^{\circ}30^{\prime}35^{\prime\prime} 779$	0.0068	0.0030	5

Note. δ_{astro} is the astrometric error. δ_{RA} and δ_{Dec} are fitting error using `imfit` for R.A. and decl., respectively. The references and ALMA project IDs are: (1) van der Marel et al. (2013), 2011.0.00635.SSB; (2) van der Marel et al. (2015), 2013.1.00100.S; (3) Francis & van der Marel (2020), van der Marel et al. (2021a), 2013.1.00100.S; (4) Ohashi et al. (2020), van der Marel et al. (2021b), 2017.1.00834.S; (5) This work, 2019.1.01059.S.

Figure 3. The errors in fitted R.A. and decl. are the square root of the sum of the squared errors from both astrometric error and fitting error. We also put 0.1 error for all epoches, which is on the order of one month. The stellar location from the Gaia proper motion measurement is also plotted, which allows us to calculate the relative displacement from the central star in panels (b) and (d). We do not consider the astrometric error from Gaia.

We note that the first two points, from van der Marel et al. (2013) and van der Marel et al. (2015), are observed at Band 9 ($440 \mu\text{m}$), whereas the others are observed at Band 7 ($870 \mu\text{m}$). Since the peak at $440 \mu\text{m}$ was reported to coincide with that at 9 mm van der Marel et al. (2015), it is reasonable to ignore the potential azimuthal displacement here, even though it was predicted in simulations with self gravity (Baruteau & Zhu 2016).¹⁰ We will use all five data points to fit the proper motion for larger sample size and time span. To highlight the difference in observing bands, we have marked the data observed at Band 9 and Band 7 with up triangles and down triangles, respectively, in all panels of Figure 3.

With these caveats in mind, we fit the proper motion of the peak after subtracting the stellar proper motion as $(-3.0 \pm 1.9, 3.0 \pm 2.5) \text{ mas yr}^{-1}$. This is $(-1.9 \pm 1.2, 1.9 \pm 1.6) \text{ km s}^{-1}$ at a distance of 136 pc and $(-0.35 \pm 0.22, 0.35 \pm 0.29) \times v_K$, whereas $v_K = 5.438 \text{ km s}^{-1}$ is the Keplerian velocity at the distance of 60 au, the location of the peak. The magnitude of the proper motion is $0.49 \pm 0.26 v_K$.

In panel (e) of Figure 3, we overplot the circular orbit and the best-fit elliptical orbit on the image. We also plot the peak locations as colorful dots with colors representing their observing epoch. We can see that the data points do not follow either a circular orbit or an eccentric orbit. There are a few possibilities that may cause this mismatch. For example, in the case of an undetected stellar companion with a nonnegligible mass (as suggested by Calcino et al. 2019), the Gaia proper motions do not take into account the possible orbital motion of the primary star. It is also possible that the crescent peak has some epicycle motion in addition to bulk orbital motion. Further work with all data sets modeled more accurately and consistently and observations toward the IRS 48 with high resolution again in 5–10 yr may help to understand the nature of the proper motion of the crescent peak.

¹⁰ We note that the 9 mm data had a much larger beam size of $0^{\prime\prime}.46 \times 0^{\prime\prime}.26$. The peaks of the emission at $440 \mu\text{m}$ and at 9 mm could still have small nonresolved displacement.

4.2. Secondary Stellar Companion?

Theoretically, one way to drive the eccentric orbital motion is to have a secondary stellar companion. In the simulation presented in Calcino et al. (2019), they introduced a companion as massive as $0.4 M_{\odot}$ at the separation of 10 au, to explain the observed asymmetry in velocity channel maps and line observations (van der Marel et al. 2016). Such a massive companion will change the mass center of the system significantly (1.67 au for their setup), and the focus of the eccentric ring should be displaced from the central star.

To explore these possibilities, we relax the constraint in Section 3.1 and introduce the location of the focus as two additional parameters. The loss function is still defined with the difference between the distances toward the new focus as its argument. There are many ellipses with similar levels of loss functions. In Figure 4, we plot 1000 orbits and their foci with reasonable fits to our data. Among these ellipses, the largest loss function is only $\sim 1\%$ larger than the smallest one. Despite the similarity in their loss functions, the location of the foci differs by almost 50 au.

The uncertainty of the fitted focus mostly comes from the dispersed nature of the emission. Deeper observations with lower noise are unlikely to give much better constraints. Aside from constraints from the dust emission, one can search for the potential secondary star with astrometry, in addition to the existing constraint from photometry (Wright et al. 2015; see discussions by Calcino et al. 2019). If there is a massive secondary stellar companion, the proper motion of the central star should have an oscillating component on the order of 1.5–2 au. If the orbit is significantly inclined, we should also observe a radial variance ($\sim 1.8 \text{ km s}^{-1}$ if the inclination is the same as the disk) with a period of about 20 yr.

Note that the discussion on the secondary stellar companion and the displaced focus will change the proper motion discussed earlier. The Keplerian velocity will change with a different total mass of the central binary system and with a different distance to the displaced focus. The system may not be super Keplerian anymore if the total stellar mass is larger. More detailed future analyses are needed to account for these additional complications.

4.3. Velocity Maps of Line Emissions

The elliptical orbit also has an impact on the velocity maps of line emission, assuming the gas is comoving with the dust. The velocity map with an eccentricity of $e = 0.27$ from our best-fit model is shown in Figure 5. We adopt a systemic velocity of 4.55 km s^{-1} as in van der Marel et al. (2021b) and

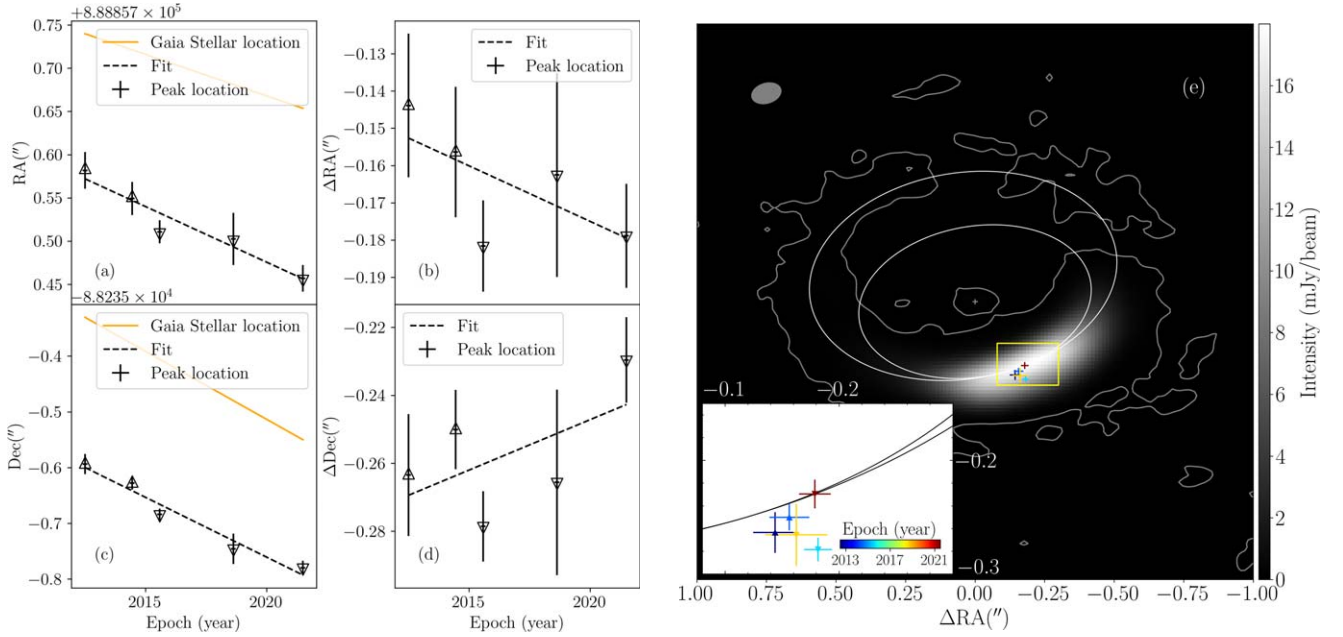


Figure 3. The R.A. (a) and decl. (c) of the crescent peak from archival ALMA data and the star assuming Gaia proper motion in units of arcseconds. The relative displacement from the assumed stellar location at each epoch is plotted in units of arcseconds in (b) and (d). The dashed lines are linear fits to each data sets. The up (down) triangles represent data points observed at ALMA Band 9 (Band 7). Panel (e): the intensity image overlaid with the predicted proper motion. The smaller and larger ellipses represent the circular and the best-fit eccentric orbit, respectively. The colorful crosses represent the fitted peak location at each epochs with errors.

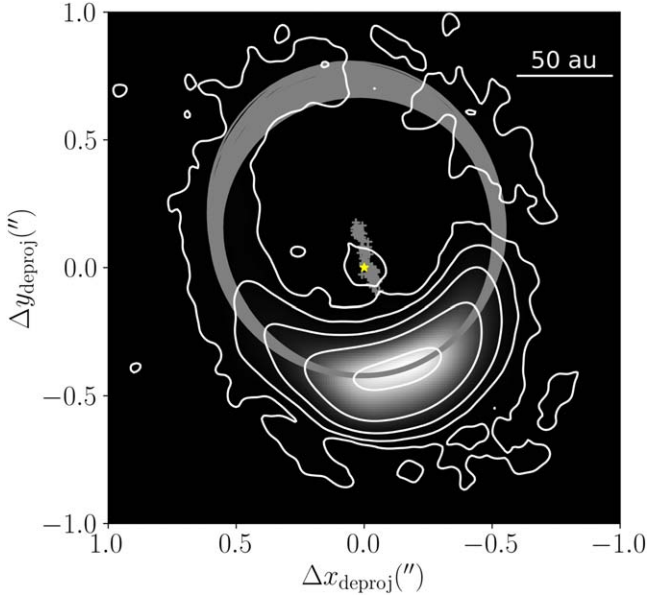


Figure 4. Orbital fits shown in the deprojected plane without using the assumption of the star at one of the foci. We plot 1000 gray ellipses with a reasonable fit. The worst of these orbits has a loss function that is only 1% larger than the best. The foci (near the star) of these ellipses are also plotted as gray crosses. The yellow star at the center marks the primary star location.

the resulting velocity map is similar to their Figure 1. In order to compare with Keplerian rotation, we also plot the isovelocity contours for the elliptical orbit as black solid lines and the contours with same levels for Keplerian rotation as black dashed lines. We can see that the red region is significantly larger than the blue region, and the redshifted solid contours are larger than their blueshifted counterparts. This is in contrast with the circular orbit, where the dashed redshifted contours are

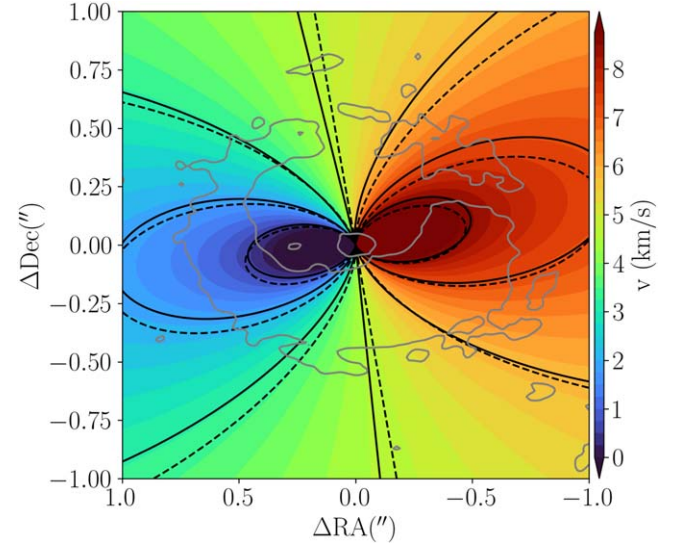


Figure 5. The velocity map of the disk, assuming an elliptical orbit with $e = 0.27$, as fitted from Section 3.1. The color bar is similar to van der Marel et al. (2021b) with $v_{\text{source}} = 4.55 \text{ km s}^{-1}$. The solid contours represent the same velocity map as the color map at the levels of $(-4, -2.67, -1.33, 0, 1.33, 2.67, 4) \text{ km s}^{-1} + v_{\text{source}}$. The dashed contours are plotted at the same velocity levels but assumes circular (Keplerian) orbit. A gray 3σ contour of the nonpolarized flux from our observation is also plotted as a background.

similar in sizes to the dashed blueshifted contours. This is because the western part of the disk is closer to the perihelion and will show larger velocities in an elliptical orbit. This asymmetry that the redshifted contours are larger than their blueshifted counterparts in velocity maps is visible in both H_2CO and ^{13}CO (van der Marel et al. 2014, 2021b), which lends support to the elliptical orbit (as first discussed by Calcino et al. 2019), although it remains to be determined whether the velocity map is quantitatively consistent with the

eccentricity of $e = 0.27$ inferred from the dust emission distribution.

5. Summary

In this work, we present deep submillimeter ALMA observations toward the transition disk IRS 48 with a high spatial resolution. The main findings are as follows:

1. For the first time, we are able to trace 95% of the ring crossing the well-known crescent-shaped structure. This ring is surprisingly eccentric with a large eccentricity of 0.27.
2. We detected compact emission at 15σ level that is centered in the star and spatially well separate from the crescent-shaped structure. The dust mass is estimated as about $1.5 \times 10^{-8} M_{\odot}$, or $0.005 M_{\oplus}$, if the emission is millimeter-sized dust thermal emission. We do not resolve the central emission with $0.1''$ beam. If the central object is an unresolved inner disk, the disk radius is a couple of astronomical units at most.
3. We fit the proper motion of the crescent-shaped dust structure as $0.49 \pm 0.26 v_K$. Existing data do not support either circular orbit or elliptical orbit. Detailed modeling and future high-resolution observations may help to understand the nature of the proper motion of the crescent peak.

We thank the referee for constructive reports that helped improve the manuscript significantly. We thank Lile Wang, Greg Herczeg, Ruobing Dong, and Pinghui Huang for fruitful discussions. H.Y. is supported by the National Key R&D Program of China (No. 2019YFA0405100) and the China Postdoctoral Science Foundation (No. 2022M710230). Z.Y.L. is supported in part by NASA 80NSSC18K1095 and NSF AST-1910106. L.W.L. and R.E.H. acknowledge support from NSF AST-1910364. Z.Y.D.L. acknowledges support from the Jefferson Scholars Foundation and the NRAO ALMA Student Observing Support (SOS) SOSPA8-003.

This paper makes use of the following ALMA data: ADS/JAO.ALMA#2019.1.01059.S, 2011.0.00635.SSB, 2013.1.00100.S, and 2017.1.00834.S. ALMA is a partnership of ESO (representing its member states), NSF (USA) and NINS (Japan), together with NRC (Canada), MOST and ASIAA (Taiwan), and KASI (Republic of Korea), in cooperation with the Republic of Chile. The Joint ALMA Observatory is operated by ESO, AUI/NRAO, and NAOJ.

ORCID iDs

Haifeng Yang (杨海峰) <https://orcid.org/0000-0002-8537-6669>

Manuel Fernández-López <https://orcid.org/0000-0001-5811-0454>

Zhi-Yun Li <https://orcid.org/0000-0002-7402-6487>

Ian W. Stephens <https://orcid.org/0000-0003-3017-4418>

Leslie W. Looney <https://orcid.org/0000-0002-4540-6587>

Zhe-Yu Daniel Lin <https://orcid.org/0000-0001-7233-4171>

Rachel Harrison <https://orcid.org/0000-0003-2118-4999>

References

- Añez-López, N., Osorio, M., Busquet, G., et al. 2020, *ApJ*, **888**, 41
- Alexander, R., Pascucci, I., Andrews, S., Armitage, P., & Cieza, L. 2014, in *Protostars and Planets VI*, ed. H. Beuther et al. (Tucson, AZ: Univ. of Arizona Press), 475
- Andre, M., & Yau, A. 1997, *SSRv*, **80**, 27
- Ataiee, S., Pinilla, P., Zsom, A., et al. 2013, *A&A*, **553**, L3
- Baruteau, C., & Zhu, Z. 2016, *MNRAS*, **458**, 3927
- Birnstiel, T., Dullemond, C. P., & Pinilla, P. 2013, *A&A*, **550**, L8
- Birnstiel, T., Dullemond, C. P., Zhu, Z., et al. 2018, *ApJL*, **869**, L45
- Brown, J. M., Herczeg, G. J., Pontoppidan, K. M., & van Dishoeck, E. F. 2012, *ApJ*, **744**, 116
- Bruderer, S., van der Marel, N., van Dishoeck, E. F., & van Kempen, T. A. 2014, *A&A*, **562**, A26
- Calcino, J., Price, D. J., Pinte, C., et al. 2019, *MNRAS*, **490**, 2579
- Dong, R., Li, S., Chiang, E., & Li, H. 2018, *ApJ*, **866**, 110
- Espaillet, C., D'Alessio, P., Hernández, J., et al. 2010, *ApJ*, **717**, 441
- Espaillet, C., Muzerolle, J., Najita, J., et al. 2014, in *Protostars and Planets VI*, ed. H. Beuther et al. (Tucson, AZ: Univ. of Arizona Press), 497
- Francis, L., & van der Marel, N. 2020, *ApJ*, **892**, 111
- Gaia Collaboration, Brown, A. G. A., Vallenari, A., et al. 2018, *A&A*, **616**, A1
- Gaia Collaboration, Vallenari, A., Brown, A. G. A., et al. 2022, arXiv:2208.00211
- Geers, V. C., Pontoppidan, K. M., van Dishoeck, E. F., et al. 2007, *A&A*, **469**, L35
- Kley, W., & Dirksen, G. 2006, *A&A*, **447**, 369
- Marsh, K. A., & Mahoney, M. J. 1992, *ApJL*, **395**, L115
- Matrà, L., Dent, W. R. F., Wilner, D. J., et al. 2020, *ApJ*, **898**, 146
- McMullin, J. P., Waters, B., Schiebel, D., Young, W., & Golap, K. 2007, in *ASP Conf. Ser. 376, Astronomical Data Analysis Software and Systems XVI*, ed. R. A. Shaw, F. Hill, & D. J. Bell (San Francisco, CA: ASP), 127
- Mohan, S., Vig, S., & Mandal, S. 2022, *MNRAS*, **514**, 3709
- Ohashi, S., Kataoka, A., van der Marel, N., et al. 2020, *ApJ*, **900**, 81
- Ragusa, E., Alexander, R., Calcino, J., Hirsh, K., & Price, D. J. 2020, *MNRAS*, **499**, 3362
- Ragusa, E., Dipierro, G., Lodato, G., Laibe, G., & Price, D. J. 2017, *MNRAS*, **464**, 1449
- Reynolds, S. P. 1986, *ApJ*, **304**, 713
- Salyk, C., Herczeg, G. J., Brown, J. M., et al. 2013, *ApJ*, **769**, 21
- van der Marel, N., Birnstiel, T., Garufi, A., et al. 2021a, *AJ*, **161**, 33
- van der Marel, N., Booth, A. S., Leemker, M., van Dishoeck, E. F., & Ohashi, S. 2021b, *A&A*, **651**, L5
- van der Marel, N., Pinilla, P., Tobin, J., et al. 2015, *ApJL*, **810**, L7
- van der Marel, N., van Dishoeck, E. F., Bruderer, S., et al. 2013, *Sci*, **340**, 1199
- van der Marel, N., van Dishoeck, E. F., Bruderer, S., et al. 2016, *A&A*, **585**, A58
- van der Marel, N., van Dishoeck, E. F., Bruderer, S., & van Kempen, T. A. 2014, *A&A*, **563**, A113
- Wright, C. M., Maddison, S. T., Wilner, D. J., et al. 2015, *MNRAS*, **453**, 414
- Zhu, Z., Stone, J. M., Rafikov, R. R., & Bai, X.-n. 2014, *ApJ*, **785**, 122